Analytic Reconstruction of the Attenuation from 3D Time-of-Flight PET Data

Ahmadreza Rezaei[1], Johan Nuyts[1], and Michel Defrise[2]

I. Introduction

In positron emission tomography (PET), an accurate quantitative reconstruction of the tracer distribution requires taking into account the attenuation of the photons by the tissues. The spatial distribution of the attenuation coefficient (the *attenuation image*) is usually estimated by means of a CT scan, extrapolated to the required photon energy of 511 keV, and forward projected to obtain the attenuation sinogram [1]. We consider applications where this external information about the attenuation is unavailable, or inaccurate due for instance to patient motion between the transmission scan and the emission scan. In such a case the attenuation must be estimated from the emission data only. Previous studies [2]–[4] have shown that time-of-flight (TOF) data contain significant information on the attenuation. Recently, we proved that the attenuation sinogram is determined, up to a constant multiplicative factor, by the 2D TOF data and that it can be calculated using an efficient analytic algorithm [5]. This paper extends this work to 3D TOF PET. Iterative algorithms dealing with the same problem are presented in [6]–[10].

II. Time-of-flight 3D PET data

We model the TOF PET data as the *TOF 3D x-ray transform* of the tracer distribution $f(x,y,z)$:

$$p(t,\phi,s,z,\delta) = \sqrt{1+\delta^2}\int_{-\infty}^{\infty} dl\, h(t-l\sqrt{1+\delta^2}) \times f(s\cos\phi - l\sin\phi, s\sin\phi + l\cos\phi, z+l\delta) \quad (1)$$

where t is the TOF variable, s and ϕ the sinogram coordinates, z the axial coordinate of the mid-point of the line of response (LOR), and the tilt $\delta = \tan\theta$ is the tangent of the angle θ between the LOR and a transaxial plane. We consider a Gaussian model for the TOF profile, $h(t) = \exp(-t^2/2\sigma^2)$. We will use the notation $\pi = (\phi, s, z, \delta)$ to denote a LOR.

The attenuation coefficient is denoted by $\mu(\vec{x})$ and the attenuation factors are $a(\pi) = \exp\{-(\mathcal{R}\mu)(\pi)\}$ with $\mathcal{R}\mu$ denoting the 3D x-ray transform of the attenuation coefficients (defined by the same equation as (1) with h replaced by 1, and f by μ). The measured data are $m(t,\pi) = p(t,\pi)a(\pi)$ and we define the set of LORs with activity as $\Omega = \{\pi = (\phi,s,z,\delta) \,|\, \exists t : m(t,\pi) > 0\}$.

We consider in this paper the problem of estimating a from the emission data m for all LORs $\pi \in \Omega$.

[1] Dept. of Nuclear Medicine, Katholieke Universiteit Leuven, B-3000, Leuven, Belgium, [2]Dept. of Nuclear Medicine, Vrije Universiteit Brussel, B-1090 Brussels, Belgium. E-mails: ahmadreza.rezaei@uz.kuleuven.be, johan.nuyts@uz.kuleuven.be and mdefrise@vub.ac.be

[3]This research is supported by a research grant (GOA) from K.U.Leuven.

III. Reconstruction of the derivatives of $\mathcal{R}\mu$

The noise-free, attenuation corrected, 3D TOF data (1) satisfy the following consistency condition [11], [12]:

$$\mathcal{D}p := \frac{\partial p}{\partial \phi} + \frac{t}{\sqrt{1+\delta^2}}\frac{\partial p}{\partial s} - s\sqrt{1+\delta^2}\frac{\partial p}{\partial t} + s\,\delta\frac{\partial p}{\partial z} + \frac{\sigma^2}{\sqrt{1+\delta^2}}\frac{\partial^2 p}{\partial s \partial t} = 0 \quad (C1)$$

Using the fact that $p = m/a$ must satisfy (C1) and that a is independent of the TOF bin t, one can show that (C1) implies

$$\mathcal{D}m + \left\{ m\frac{t}{\sqrt{1+\delta^2}} + \frac{\sigma^2}{\sqrt{1+\delta^2}}\frac{\partial m}{\partial t}\right\} G + m\,H = 0 \quad (2)$$

where $G = \partial\mathcal{R}\mu/\partial s$ and $H = \partial\mathcal{R}\mu/\partial\phi + s\delta\,\partial\mathcal{R}\mu/\partial z$ are independent of t, and where the quantities $\partial m(t,\pi)/\partial t$ and $\mathcal{D}m(t,\pi)$ can be calculated by differentiating the measured data m.

The TOF data satisfy in addition to (C1) a second independent consistency condition for TOF-PET [11]:

$$\mathcal{K}p := \frac{\partial p}{\partial \delta} - \frac{t}{\sqrt{1+\delta^2}}\frac{\partial p}{\partial z} + \frac{t\delta}{1+\delta^2}\frac{\partial p}{\partial t} - \frac{\sigma^2}{\sqrt{1+\delta^2}}\frac{\partial^2 p}{\partial z \partial t} + \frac{\delta\sigma^2}{1+\delta^2}\frac{\partial^2 p}{\partial t^2} = 0 \quad (C2)$$

Applying to C2 the same method as above implies

$$\mathcal{K}m - \left\{ m\frac{t}{\sqrt{1+\delta^2}} + \frac{\sigma^2}{\sqrt{1+\delta^2}}\frac{\partial m}{\partial t}\right\} U + m\,V = 0 \quad (3)$$

where $U = \partial\mathcal{R}\mu/\partial z$ and $V = \partial\mathcal{R}\mu/\partial\delta$ are independent of t and $\mathcal{K}m(t,\pi)$ can be calculated from the measured data m.

Consider a fixed LOR $\pi \in \Omega$. Requiring that (2 and 3) must be satisfied for all TOF bins t, the quantities $G(\pi)$, $H(\pi)$, $U(\pi)$ and $V(\pi)$ can be estimated by a least-square fit at fixed π. This allows a unique estimation of the spatial derivatives of the attenuation sinogram ($\mathcal{R}\mu$) from the emission measurements ($m(t,\pi)$).

IV. Reconstruction of $\mathcal{R}\mu$

The procedure in section III yields an estimate of the gradient of ($\mathcal{R}\mu$) with respect to the four variables ϕ, s, z, δ. One is then left with the problem of integrating the gradient within the region Ω of "active" LORs to recover the attenuation factors a required to reconstruct the tracer distribution. We use a four step approach: i/ apply rebinning to the radial derivative $G = \partial\mathcal{R}\mu/\partial s$, ii/ integrate the radial derivative separately in each direct plane $z, \delta = 0$ using the method in [5], iii/

reconstruct the attenuation map μ, iv/ reproject μ along all oblique ($\delta \neq 0$) LORs.

John's consistency equation [13] for the 3D x-ray transform of the attenuation coefficients is given by,

$$\mathcal{J}(\mathcal{R}\mu) := \frac{\partial^2}{\partial z \partial \phi}\left(\frac{(\mathcal{R}\mu)}{\sqrt{1+\delta^2}}\right) + \frac{\partial^2}{\partial \delta \partial s}\left(\frac{(\mathcal{R}\mu)}{\sqrt{1+\delta^2}}\right) + s\,\delta\,\frac{\partial^2}{\partial z^2}\left(\frac{(\mathcal{R}\mu)}{\sqrt{1+\delta^2}}\right) = 0 \quad \text{(C3)}$$

In step i/, the approximate Fourier rebinning (FORE) algorithm for the radial derivative $G = \partial \mathcal{R}\mu / \partial s$ is derived by differentiating w.r.t. s John's consistency equation, by taking the Fourier transform, and by neglecting terms of order δ. The result is identical to the usual FORE [14]:

$$\begin{aligned} \hat{G}_{reb}(\omega, k, z_0) &:= \hat{G}(\omega, k, z_0, 0) \quad (4) \\ &\simeq \frac{1}{\delta_b - \delta_a}\int_{\delta_a}^{\delta_b} d\delta\, \hat{G}(\omega, k, z_0 + (k/\omega)\delta, \delta) \end{aligned}$$

with $\hat{G}$ the 2D Fourier transform of G w.r.t. s and ϕ, and $[\delta_a, \delta_b]$ the range of the polar angle (the integral over δ is implemented as a sum over all "segments"). In contrast with the usual FORE, no special handling of the low radial frequencies is required because $\hat{G}(0, k, z_0, \delta) = 0$.

Furthermore, the consistency condition of C3 can be written by the estimated parameters G and H as,

$$\frac{\partial G}{\partial \delta} + \frac{\partial H}{\partial z} = 0 \quad (5)$$

Integration over the tilt angle δ and over all the possible range of the polar angles $[\delta_a, \delta_b]$ gives an estimate of the exact rebinned radial derivative sinogram as,

$$\begin{aligned} G_{reb}(\phi, s, z_0) &:= G(\phi, s, z_0, 0) \quad (6) \\ &= \frac{1}{\delta_b - \delta_a}\int_{\delta_a}^{\delta_b} d\delta \{G(\pi) + W(\delta)\frac{\partial}{\partial z}H(\pi)\} \end{aligned}$$

with,

$$W(\delta) = \begin{cases} \delta_b - \delta & \delta > 0 \\ \delta_a - \delta & \delta < 0 \end{cases}$$

V. Experimental Design and Results

We first analyze the reconstructions of the rebinning algorithms using simulations of the NCAT phantom (figure 1). Then, we study the methods using a 5 minute scan of the NEMA IEC body phantom with 6.18 mCi injection scanned 2 hours post injection.

A. Comparison of Rebinning Algorithms

For this study, the NCAT phantom was put close to the edge of the field-of-view of the PET scanner. 5D TOF emission data were generated and organized in 200 radial bins, 168 azimuthal angles, 5 co-polar angles, 13 time-bins of 312 ps width and with an effective TOF resolution of 580 ps. The attenuation volume was then reconstructed in a 200×200×81 volume. TOF PET sinograms were simulated varying the span of the scanner to study the effectiveness of the exact rebinning algorithm with respect to the approximate FORE rebinning algorithm. Least square estimates of G and H derivatives were computed from equation 2 as in [5] and these estimates were then rebinned into direct planes using the approximate FORE and the exact method defined in equations 4 and 6 respectively.

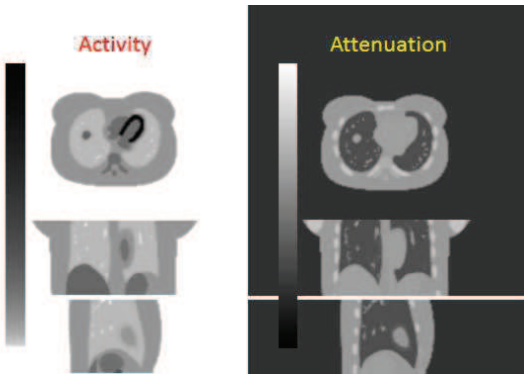

Fig. 1. Transaxial (top), coronal (center) and sagittal (bottom) views of activity (left) and attenuation (right) of the NCAT phantom.

In this study, we compare the reconstructions of the eleventh segment of a scanner with a span of 3 with the reconstruction of the third segment of a scanner with a span of 11 (the two oblique segments have the same tilt angle). We assumed that the measurements of cross coincidence detector pairs can be modelled by a single detector pair with a tilt angle equal to the average of all the tilt angles. Figure 2 shows the attenuation reconstructions of these two scanners when the data are rebinned using the approximate FORE and the exact methods respectively. Note that the reconstructions have not been corrected for the missing constant in the attenuation sinogram.

From figure 2, we find that the exact rebinning algorithm is able to give an accurate estimate of the axial attenuation profile when a fine axial sampling (small span) was available. In practice however, we find that the approximate FORE rebinning algorithm is able to deliver better results due to the poor axial sampling of the scanners and the additional derivative needed for the exact rebinning algorithm (which will be demonstrated later). It can be seen that the errors due to this poor axial sampling tend to increase as the distance of the attenuating object increases from the center of the FOV of the scanner.

B. NCAT Phantom

In this study, we used the TOF emission data of the NCAT phantom, figure 1, to assess the quality of the attenuation reconstructions in realistic situations. The phantom was located in the center of the PET FOV, we used a span of 11 for the study (same scanner specifications as the Siemens Biograph mCT) and reconstructions of the attenuation volume were made for all possible tilt angles. Unlike the first study, the TOF measurements were simulated using all cross coincidence detector pairs.

Here we compare the attenuation reconstruction of the two rebinning algorithms, exact and approximate FORE, to an attenuation reconstruction where the uncorrected emission data are first rebinned to direct planes using the existing TOF-SSRB algorithm and then the G and H derivatives are computed

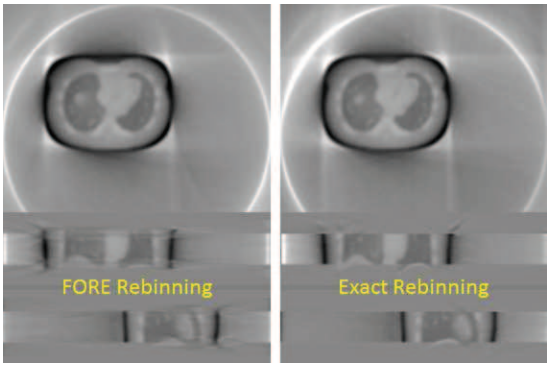

a) Span=3, Segment=11.

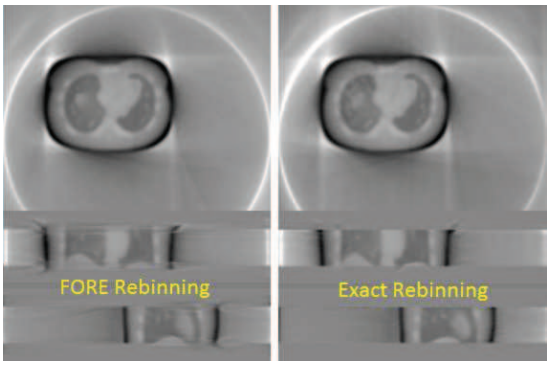

b) Span=11, Segment=3.

Fig. 2. Attenuation reconstruction of the eleventh segment of a scanner with a span of 3 (top) and the third segment of a scanner with a span of 11 (bottom). Transaxial, coronal and sagittal views of reconstructions with the approximate FORE rebinning (left) and the exact rebinning (right) algorithms.

for each direct plane (setting $\delta = 0$). We correct for the missing constant in each plane separately by assuming tissue attenuation in the central region of the NCAT phantom. Figure 2 shows the attenuation reconstructions in transaxial and axial planes.

It can be seen that when the rebinning is done with TOF-SSRB prior to computing the G and H derivatives the reconstructed attenuation suffers from excessive smoothness. This is due to the fact that the attenuation values differ for oblique and direct lines of response which is neglected when the uncorrected emission data are first rebinned into direct planes. Although we saw differences in the axial resolution of the two exact and approximate rebinning algorithms for the off-center NCAT phantom, the difference does not appear to be very significant in more realistic phantom simulations. This is in part due to the position of the phantom (located in the center of the FOV) and due to modelling all the possible cross coincidence detector pairs in the TOF emission measurements which leads to smoothness of the attenuation reconstruction in the axial direction. The G and H derivative estimates are inaccurate near the boundary of the object [5]. The effect of this inaccuracy near the object boundaries can be seen as streak-like artifacts around the reconstructed object (better seen in the attenuation reconstructions from noisy data).

Poisson noise was added to the measurements to analyze the behaviour of the methods under noisy conditions. The maximum count in the 3D TOF emission data was 22 and the

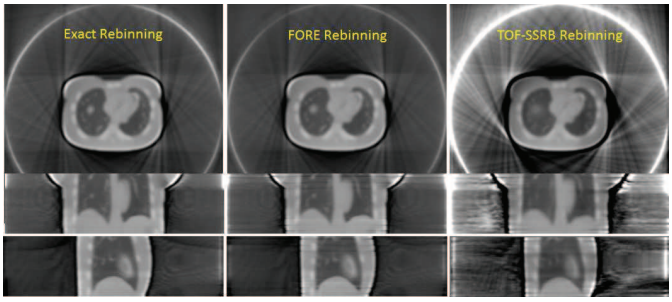

Fig. 3. Transaxial (top), coronal (center) and sagittal (bottom) views of the attenuation reconstructions from noise-less emission data. 2D FBP reconstructions of the integrated radial derivative obtained by i/ applying the exact (left) and the approximate FORE (middle) rebinning to the G and H derivatives estimated using (2) and ii/ applying the 2D method of [5] to the 2D data obtained by TOF-SSRB rebinning of the uncorrected 3D emission data.

corresponding non-TOF emission data had a maximum of 40 counts. We found that a small amount of sinogram smoothing leads to significant noise reduction in the G and H derivative estimates and hence in the attenuation reconstruction of the approximate FORE and exact methods. However, in the TOF-SSRB method we omitted this sinogram smoothing. Figure 3 shows the attenuation reconstructions of noisy emission data in transaxial and axial planes after post-smoothing with a 1cm FWHM Gaussian.

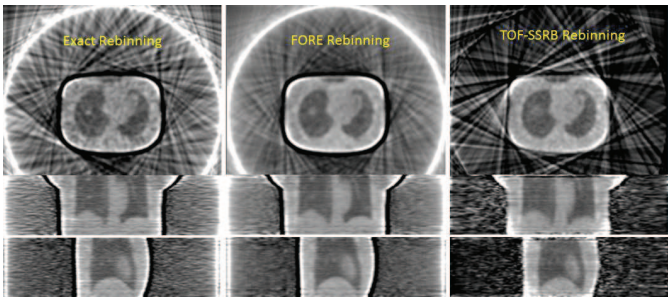

Fig. 4. Transaxial (top), coronal (center) and sagittal (bottom) views of the attenuation reconstructions from noisy emission data. 2D FBP reconstructions of the integrated radial derivative obtained by i/ applying the exact (left) and the approximate FORE (middle) rebinning to the G and H derivatives estimated using (2) and ii/ applying the 2D method of [5] to the 2D data obtained by TOF-SSRB rebinning of the uncorrected 3D emission data.

We observed that the two exact and approximate FORE methods produced similar attenuation images with different noise profiles in the reconstructed attenuation volumes. The attenuation reconstruction of the exact rebinning method look noisier than the attenuation reconstructions of approximate FORE. This noise amplification was anticipated and is due to the additional derivative required in the exact rebinning algorithm. Just as before, when the rebinning is done prior to computing the G and H derivatives (TOF-SSRB reconstructions) the reconstructed attenuation suffers from excessive smoothness which was caused by incorrectly averaging over the counts of oblique LORs. However due to this incorrect averaging, the attenuation reconstruction suffers less from noise in the TOF emission data.

C. NEMA IEC Body Phantom

The TOF emission data of the NEMA IEC body phantom were used to estimate the G and H derivatives. The emission data were first compensated for detector sensitivities and then the scatter and randoms contributions were subtracted from the emission sinogram prior to the estimation of the derivatives. The rebinned radial derivative was computed by the approximate FORE and the exact rebinning methods and the attenuation volume was reconstructed from the rebinned sinograms. Figure 5 shows the OSEM reconstruction of the activity and the FBP reconstruction of the attenuation from the CT together with the attenuation estimates computed only from the emission data, using the approximate FORE and the exact rebinning methods.

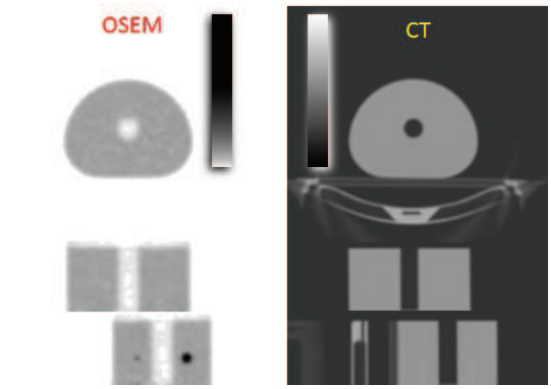

a) OSEM activity and FBP attenuation from CT.

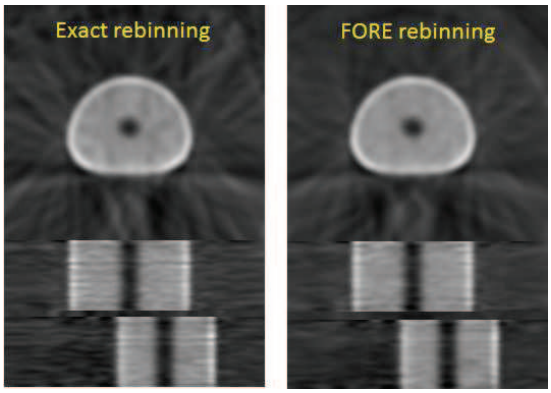

a) Exact and approximate FORE FBP attenuation reconstructions.

Fig. 5. Transaxial, coronal and sagittal views of the NEMA IEC body phantom activity (top-left) and CT attenuation (top-right) images. 2D FBP reconstructions of the integrated radial derivative obtained by applying the exact (bottom-left) and the approximate FORE (bottom-right) rebinning to the G and H derivatives estimated using (2).

Figure 5 shows the attenuation reconstructions of the NEMA IEC phantom in an axial plane with more details in the attenuation image. Although the exact attenuation values of the bed could not be reconstructed from the emission data, it can be seen that more attenuation is put along the direction of LORs that see the higher bed attenuating values. The attenuation reconstructions shown in figure 5 have been corrected for the missing constant similar to [5].

VI. Discussion and Conclusion

Recently it was shown that time-of-flight emission data determine the attenuation sinogram up to a constant term. In [5] an algorithm was proposed that estimates the 2D attenuation sinogram from its radial and angular derivatives. This study is the extension of the latter to 3D where we only make use of the radial derivative to estimate the attenuation volume and sinogram. We analyze the effect of exact and approximate rebinning of the derivative sinograms and find that the accuracy of these algorithms depends on the span used in different TOF PET systems. Although the exact method does not require 2D FFT computations, we find that in practice the approximate FORE rebinning algorithm is able to deliver better results. This is due to poor scanner axial samplings and the additional derivative needed for the exact rebinning algorithm which results in noise magnification in our reconstructions. We see that rebinning of the TOF emission data (TOF-SSRB) and finding the estimation of the radial derivative in the direct plane results in severe smoothness in the attenuation image and thus in the attenuation sinogram. We were able to reconstruct relatively good attenuation estimates from relative noisy TOF measurements. However, the usefulness of these attenuation estimates for attenuation correction of the PET data is to be quantitatively analyzed.

References

[1] PE Kinahan *et al.*, 1998 Attenuation correction for a combined 3D PET/CT scanner, *Med Phys* **25 (10)** 2046-2053
[2] TG Turkington *et al.*, 2009 Attenuation artifacts and time-of-flight PET, *Record Nuclear Science Symposium Conference (NSS/MIC)* 2297-2299.
[3] M Conti, 2011 Why is TOF PET reconstruction a more robust method in the presence of inconsistent data?, *Phys Med Biol* **56** 155-168
[4] A Salomon *et al.*, 2011 Simultaneous Reconstruction of Activity and Attenuation for PET/MR, *IEEE Trans Med Imag* **30** 804-813
[5] M Defrise *et al.*, 2012, Time-of-flight PET data determine the attenuation sinogram up to a constant, *Phys. Med. Biol.* **57**, 885899
[6] A Rezaei, *et al.*, 2011 Simultaneous reconstruction of activity and attenuation in Time-of-flight PET, *Records 2011 IEEE Nuclear Science Symposium and Medical Imaging Conference, Valencia*, p. 2375-2382.
[7] A Rezaei, *et al.*, 2012 Simultaneous reconstruction of activity and attenuation in Time-of-flight PET, *IEEE Trans. Med. Imag.*, In press.
[8] J Nuyts, *et al.*, 2012 ML-reconstruction for TOF-PET with simultaneous estimation of the attenuation factors, *2012 IEEE Nuclear Science Symposium and Medical Imaging Conference, Anaheim*, paper M04-1.
[9] V Panin, *et al.*, 2012 Reconstruction of Uniform Sensitivity Emission Image with Partially Known Axial Attenuation Information in PET-CT Scanner, *2012 IEEE Nuclear Science Symposium and Medical Imaging Conference, Anaheim*, paper M04-7.
[10] J Hamill, 2012 TOF-MLAA for Attenuation Correction in Thoracic PET/CT, *2012 IEEE Nuclear Science Symposium and Medical Imaging Conference, Anaheim*, paper M23-1.
[11] M Defrise *et al.*, 2008 Continuous and Discrete Data Rebinning in Time-of-Flight PET, *IEEE Trans. Med. Imag.* **27** 1310-1322.
[12] M Defrise *et al.*, New consistency equation for time-of-flight PET, *Records 2011 IEEE Nuclear Science Symposium and Medical Imaging Conference, Valencia*, p. 4115-4120.
[13] M Defrise, *et al.*, 1999 A fast rebinning algorithm for 3D positron emission tomography using John's equation, *Inverse Problems*, 15(4):1047-1065.
[14] M Defrise, *et al.*, 1997 Exact and Approximate Rebinning Algorithms for 3-D PET Data, *IEEE Trans. Med. Imag.*, 16(2):145-158.